The preparation and catalytic performance of graphene-reinforced ion-exchange resins

Journal:	*RSC Advances*
Manuscript ID:	RA-ART-08-2014-008972.R2
Article Type:	Paper
Date Submitted by the Author:	25-Sep-2014
Complete List of Authors:	Li, Yanan; Sinopec Shanghai Research Institute of Petrochemical Technology (SRIPT), Yu, Fengping; Sinopec Shanghai Research Institute of Petrochemical Technology (SRIPT), He, Wenjun; Sinopec Shanghai Research Institute of Petrochemical Technology (SRIPT), Yang, Weimin; Sinopec Shanghai Research Institute of Petrochemical Technology (SRIPT),

Journal Name

RSCPublishing

ARTICLE

The preparation and catalytic performance of graphene-reinforced ion-exchange resins

Cite this: DOI: 10.1039/x0xx00000x

Received 00th January 2012,
Accepted 00th January 2012

DOI: 10.1039/x0xx00000x

www.rsc.org/

Yanan Li, Fengping Yu, Wenjun He and Weimin Yang[a] ,

Graphene-based polymer nanocomposites (GPNCs) were prepared by *in situ* suspension polymerization and the prepared polymers were chloromethylated with chloromethyl ethyl ether and then aminated with trimethylamine to obtain graphene-based nanocomposite ion-exchange resins (GPNC-IERs). Raman spectroscopy revealed the existence of chemical bonded interaction between graphene and the polymer networks *via* the increased intensity and shift in the vibration bands of graphene in the nanocomposites. The reinforced thermal and structural properties of the nanocomposites were investigated with graphene amounts from 0 to 1.0 wt%. The thermal stability was evaluated by thermogravimetric-differential thermal analysis (TG-DTA). It showed that the addition of graphene to the polymer matrix greatly increased the onset degradation temperature by 20 °C. The structural properties of the nanocomposites such as swelling capacity and total exchange capacity were improved with 0.4 wt% graphene, which confirmed that the good dispersion of graphene throughout the polymer matrix with strong interaction within the polymer networks played an important role in the properties enhancement effect. With the excellent anti-swelling property and thermal stability, the GPNC-IER catalysts presented a better performance in hydration of ethylene oxide (EO) to monoethylene glycol (MEG) including reaction activity, selectivity and stability in 500 h tests.

Introduction

Monoethylene glycol (MEG) is an important intermediate for the production of polyethylene terephthalate (PET). Generally, MEG is produced predominantly by non-catalytic liquid-phase hydration of ethylene oxide (EO) with significant amounts of by-products diethylene glycol (DEG) and triethylene glycol (TEG). In order to obtain high selectivity of MEG, a large excess amount of water (about 20-25 molar ratio of water/EO) must be used industrially, which increases production cost due to energy consumption and distillation unit operation investment.[1,2] Therefore, many academic and industrial researchers have focused on the catalysts for EO hydration to MEG at low water/EO molar ratio, for instance, anions of salts (such as acetate, formate, carbonate and bicarbonate) immobilized on ion-exchange resins (IERs),[3-7] quaternary phosphonium halides,[8] polymeric organosilane ammonium salts,[8,9] macrocyclic chelating compounds and supported metal oxides.[10-12] In addition, immobilized IER is considered to be one of the best catalysts because of its excellent reaction performance and easy separation progress. Shvets *et al.*[5] reported that under a reaction temperature of 95 °C and a water/EO molar ratio of 18, the EO conversion and MEG selectivity on the IER catalysts exhibited 95.6% and 98.1%, respectively. However, the instinct drawbacks of the ion-exchange polymers, such as swelling and deactivation of IERs under reaction condition, restrict their further industrial application. Higher crosslinking density helped with reducing the swelling at a cost of ion-exchange capacity and reactive sites of the IER catalysts.[4,13-16] Xie *et al.*[17] have reported the use of carbon nanotubes (CNTs) as a reinforcing filler in polymer composites to deal with the swelling problem of the IERs. It was found that the anti-swelling capacities and thermal stability of the polymer/CNTs composites had been improved, and the catalysts performed well in the EO hydration reaction test.

Recently, graphene has played an important role in nanoscience owning to its exceptional mechanical, electrical, chemical and thermal properties.[18-21] Its mechanical strength is comparable to that of CNTs and the two-dimensional honeycomb layer of sp^2-boned structure has potential applications in many fields as composite materials, energy storage and conversion, sensors and nanoscale electronic components, *etc*. Recent studies have reported that the scalable production cost of graphene sheets in large quantities could be much lower than CNTs, which might rival the CNTs in many technological applications.[18,19] Graphene-based polymer nanocomposites (GPNCs) have attracted considerable interest in order to enhance multifunctional properties of polymer matrix. As a reinforcing phase, graphene sheets should be incorporated and distributed homogenously into various polymer matrices. However, graphene could form aggregation due to the strong van der Waals forces and π-π interactions between the layers.[21] To obtain the well dispersed graphene in the polymer matrix, many methods have been developed to reduce the aggregation, including solvent-based exfoliation, ultrasonication with surfactant and chemical functionalization. Chemical converted graphene sheets or graphene oxide could readily form stable dispersions in the organic solvents. However, it was found that chemical modification couldn't provide a good control of polymer architecture,[22] and additional reduction procedure is required using hydrazine as a chemical reducing agent, which is not environmentally friendly.[23,24]

To the best of the authors' knowledge, there are limitied reports describing the synthesis and properties of well-defined graphene-based nanocomposite ion-exchange resins (GPNC-IERs) by *in situ* suspension polymerization. This work employed the modified *in situ* suspension polymerization approach to prepare several strong basic GPNC-IERs without any surfactant. Then, the as-prepared GPNC-IER composites were characterized by scanning electron microscopy (SEM), Raman spectroscopy, Fourier transform infrared (FTIR) spectroscopy, X-ray photoelectron spectroscopy (XPS), thermogravimetric-differential thermal analysis (TG-DTA), differential scanning calorimetry (DSC) and the measurement of anti-swelling properties. The effects of graphene acting as a reinforcing phase in the resins and those of exchange capacity, thermal stability and catalytic performance are conducted with reference to the incorporation and interaction of graphene within the polymer networks.

Experimental Section

Materials

Styrene (St, Sinopharm Chemical Reagent Co., Ltd., 99%) and divinylbenzene (DVB, Sigma-Aldrich Chemicals, technical grade, 80%) were washed by NaOH solution (5 wt%) thrice to remove inhibitors, then washed with deionized water, stirred over magnesium sulfate overnight and then over calcium hydride, distilled, and stored under a nitrogen atmosphere at 4 °C. The purification of radical initiator benzoyl peroxide (BPO; Sinopharm Chemical Reagent Co., Ltd., 98%) was prepared by recrystallization from methanol solution. Chloromethyl ethyl ether (96%) was purchased from Tokyo Chemical Industry Co., Ltd. Other chemicals including gelatin (CP), zinc chloride ($ZnCl_2$, AR), tetrahydrofuran (THF, AR), trimethylamine hydrochloride (98%) and 1,2-dichloroethane (99%) were purchased from Sinopharm Chemical Reagent Co., Ltd., and used as received. Pristine graphene (Nanjing JCNANO Technology Co., Ltd., JCGNP-15-10, 99.5%) was calcined to remove amorphous carbon at 110 °C for 1 h in air.

Synthesis of the GPNCs and GPNC-IERs

Graphene was suspended in 10 mL styrene monomer, and then ultrasonicated for 10 min to obtain the required dispersions. 2.5 g gelatin was dissolved in 200 mL deionized water at 40 °C in a 500 mL round-bottom flask. The monomer mixture consisted of 45.3 g St, 4.4 g DVB, 0.5 g BPO and the prepared graphene suspension. The suspension polymerization was carried out in the presence of the monomer mixture at the organic-aqueous interface with whole-process stirring. After 30 min pre-blending at 40 °C, raised temperature gradually to 70 °C and maintained for 1 h. The polymerization occurred and proceeded at 80-85 °C for 6 h and then at 95-97 °C for 4 h. The polymer composite precipitated out as beads, which was then separated and washed by hot deionized water. The obtained GPNC was dried at 90 °C and designated as X-GEP (X defined as the weight content of graphene from 0.1 up to 1.0 wt%). For instance, sample 0.1-GEP indicates the graphene content in the nanocomposite is 0.1 wt%.

After polymerization, the Friedel-Craft reaction was carried out to introduce chloromethyl groups to the cross-linked networks of the GPNCs. The composite (25.0 g) and chloromethyl ethyl ether (75 mL) were mixed to swell the cross-linked polymer for 2 h at room temperature. Then, $ZnCl_2$ (9.6 g) was added to the mixture in two batches. The reaction was allowed to proceed at 38-40 °C for 10 h. The chloromethylation product (designated as X-GEP-Cl) was washed by acetone and dried until a constant weight was reached. Then trimethylamine hydrochloride was added to the products in three batches and the amination reaction ran for 6 h at 30 °C. After the reaction, the product was washed by deionized water, NaOH and $NaHCO_3$ aqueous solution to obtain the strong basic IERs in hydroxylic and bicarbonate form (designated as X-GEP-OH and X-GEP-HC). Schematic diagram of preparation steps of the GPNC-IERs is shown in **Scheme 1**.

As a comparison, styrene-divinylbenzene cross-linked polymer IERs were also synthesized using the same procedure in the absence of graphene. The products were designated as PS-DVB, PS-DVB-Cl, PS-DVB-OH and PS-DVB-HC, respectively. All the polymer IERs with a crosslinking density (*CD*) of 6% were controlled and presented according to the following equation (1).[25]

$$CD\ (\%) = \frac{m(\text{DVB})}{m(\text{St}) + m(\text{DVB})} \times 100\% \qquad (1)$$

Characterization and measurement

Scanning electron microscopy (SEM, Philips XL30E) was used to observe the general size and surface morphology of the polymer beads. The samples were coated with a thin layer of gold on the surface. The pressure during scanning was 5.2×10^{-9} MPa and the accelerated voltage was 5 kV. Fracture surface of the nanocomposites were observed by a FEI Nova NanoSEM 450 instrument with accelerating voltage of 5 kV. The Raman spectra were collected with LabRam-1B micro-Raman spectrometer (Jobin Yvon Instrument), using the He-Ne laser excitation line at 632.8 nm. Acquisition time was 30 s with a final laser power of about 3 mW at the surface. Fourier transform infrared (FTIR) spectra were obtained in dried KBr pellets (1:49 sample-to-KBr mass ratio) on Nicolet 5700 spectrometer (ThermoElectron, Madison, WI, US). All the spectra were recorded at a range of 4000-400 cm^{-1} with 32 scans and a resolution of 4 cm^{-1} by subtracting the background spectra, and such difference spectra are reported herein. The X-ray photoelectron spectroscopy (XPS) experiments were carried out on a Kratos AXIS Ultra DLD (Shimadzu Corporation, Kyoto, Japan) spectrometer using a monochromatic Al Kα

($h\nu$=1486.6 eV) irradiation source at 75.0 W. All XPS spectra were recorded with pass energy of 80 eV for the survey spectra, and 40 eV for high resolution spectra. The samples were directly pressed to a self-supported disk (10 10 mm^2), mounted onto a sample holder, and then degassed overnight in the vacuum chamber. The binding energies were calibrated with the containment carbon (C_{1s}=284.8 eV). Thermogravimetry-differential thermal analysis (TG-DTA) was performed on a TA Instruments SDT Q600 TGA thermogravimetric analyzer from room temperature to 900 °C at a heating rate of 10 °Cmin under a dynamic (100 mL·min^{-1}) air or N_2 atmosphere. The differential scanning calorimetry (DSC) cycling curves were measured with DSC Q2000 (TA Instruments-Waters LLC, USA) in 50 mL·min^{-1} N_2 as the purge gas at a rate of 10 °C·min^{-1}. The procedures of each DSC run were as follows: heat from room temperature to 200 °C, then hold isothermal at 200 °C for 5 min, cool equilibrated to 50 °C, and then heat from 50 °C to 160 °C. Samples of approximately 7-9 mg in these examinations were weighed with a precision of 0.01 mg aluminium pans prior to analysis. All measurements were repeated at least twice.

The as-prepared resins were characterized by various structural parameters such as swelling capacity (*SC*), water retention capacity (*A*), mean mesh size (D_v), average mesh density (ρ) and total exchange capacity (*Q*). The swelling capacity was determined through the procedures given below. The resins were immersed in deionized water for 24 h and dried at 60 °C for 72 h. The volumes of the resins were recorded after the drying process as V_a. As mentioned above, the anti-swelling property of the IER catalysts are crucial to the catalytic hydration of EO. The swollen volumes in various solvent systems were measured as V_s. The swelling capacity in the solvents were calculated according to equation (2).[26]

$$SC\ (\%) = \frac{V_s\text{-}V_a}{V_a} \times 100\% \tag{2}$$

For evaluating the catalytic performance, total exchange capacity of the prepared resins were measured according to National Standard of People's Republic of China GB/T 5760-2000, which describes the determination of the exchange capacity of anion-exchange resins in hydroxylic form.[13] The methodology was as follows: the sample was first pre-treated according to National Standard of People's Republic of China GB/T 5476. Then it was washed with HCl aqueous solution (2 mol·L^{-1}), deionized water, and NaOH aqueous solution (2 mol·L^{-1}) in sequence. The sample was measured and soaked in 100 mL standard HCl solution at 40 °C for 2 h, then 25 mL soaked solution was titrated with standard NaOH solution using phenolphthalein as the indicator. The total exchange capacity (*Q*) was calculated according to equation (3).

$$Q = \frac{100c_1 - 4c_2V_t}{W(1\text{-}A)} \tag{3}$$

Where c_1 is the molar concentration of standard HCl solution, c_2 is the molar concentration of standard NaOH solution. The volume of the titrating solution of NaOH was recorded as V_t, while W is the weight of the IER sample. A is the water retention capacity of the sample measured by National Standard of People's Republic of China GB/T 5759-2000.

Catalytic application in hydration of EO

The prepared GPNC-IERs and PS-DVB IER were applied in hydration reaction of EO. Typically, the IER catalysts were placed in a fixed bed reactor with a dimension of 10 mm (i.d.) × 300 mm (length). The experiments were carried out with a liquid hourly space velocity of 3 h^{-1} (water/EO molar ratio of 10) under pressure of 1.2 MPa in the temperature range of 90-102 °C. The composition of effluent product was analyzed by a gas chromatograph (Agilent 7890A GC) equipped with a 30 m (length) × 0.25 mm (i.d.) × 0.25 μm (film) HP-INNOWAX capillary column and a flame ionization detector (FID). Both EO conversion and MEG selectivity were taken into account as the criterion for comparison of IER catalysts' performance in this study.

$$X_{\mathrm{EO}}\ (\%) = \frac{n(\mathrm{MEG}) + 2n(\mathrm{DEG}) + 3n(\mathrm{TEG})}{n_0(\mathrm{EO})} \times 100\% \tag{4}$$

$$S_{\mathrm{MEG}}\ (\%) = \frac{n(\mathrm{MEG})}{n(\mathrm{MEG}) + 2n(\mathrm{DEG}) + 3n(\mathrm{TEG})} \times 100\% \tag{5}$$

Where n(MEG), n(DEG) and n(TEG) are the molar compositions in the effluent product, and n_0(EO) is the molar composition of EO in the feed.

Results and discussion

Morphology of the GPNCs and GPNC-IERs

Various graphene-based polymer composites were prepared *via* the modified suspension polymerization. The quality of graphene dispersion in the monomer during polymerization not only affects the further dispersion in the polymer matrix, but also directly correlates with their effectiveness for improving thermal, anti-swelling and other properties. The dispersion stability against van der Waals aggregation of graphene in styrene for 2 h was compared in **Fig. 1**. After the mixture was ultrasonicated for 10 min, it appeared that graphene could disperse well in styrene. Although some particulates were settled to the bottom of the vials over 2 h, graphene stayed homogenously for at least 30 min. Moreover, graphene shows better dispersion behavior at low concentration ([graphene] ≤ 0.7 mg·mL^{-1}) even after several hours. For example, a graphene suspension with 1 h ultrasonication at a low concentration of 0.1 mg·mL^{-1} was stable for more than 12 h. At higher concentration, the suspension was found to have lower stability, and some graphene particulates were settled to the bottom of the vial. This indicates that the equilibrium aggregation of graphene could be controlled and the concentration of graphene in the suspension is critical. The highly stable graphene suspension in monomer is possibly related to strong interactions between graphene and monomer, thus favoring the homogeneity of the beads during the suspension polymerization.

Fig. 2 presented the SEM micrographs of the polymer beads and IERs in chloric and bicarbonate form. By suspension polymerization, graphene was proximately homogeneous dispersing in the monomer and bound in or to polymer cross-linked structure gradually with the elevated temperature without causing aggregation. Therefore, the GPNCs resulted in very fine beads with spherical shapes as well as PS-DVB, and the size of the beads was in the same range of 400-600 μm. **Fig. 2** also showed the surface morphologies of the GPNC-IERs. The structure of GPNCs obviously changed from smooth sphere with homogeneously dispersed graphene to the beads with some crumpled cracks and isolated patches on the surface when the graphene content reached 1.0 wt%. These results indicate that graphene had an optimum content in the polymer networks.

High-resolution SEM images of the fracture surface of GPNCs were shown in **Fig. 3**. In the case of 0.4-GEP, graphene was well dispersed throughout the matrix, without agglomerates formed during the polymerization. More importantly, as seen in the **Fig. 3(a)**, graphene was completely separated in pieces and tightly embedded in the matrix, suggesting the excellent dispersion and compatibility of graphene within the polymer matrix. For the SEM image of 1.0-GEP, some graphene sheets exhibited a stack on the fracture surface, showing the formation of defects and higher roughness on the fracture surface. These SEM results revealed that lower graphene contents in GPNCs could effectively prohibit the restacking of graphene, providing the strengthened interfacial interaction and a graphene-polymer 3D-network.

TEM results also confirmed the well dispersed graphene in the polymer in **Fig. 4**. Pristine graphene exhibited a wrinkled morphology with lamellar structure. **Fig. 4(b)** showed the 0.4-GEP consisted of single-to-few layer graphene closely associated with the polymer, forming the strong interfacial action within the polymer matrix.

Structural properties of the GPNCs and GPNC-IERs

The Raman spectra of pristine graphene, PS-DVB and GPNCs were plotted in **Fig. 5**. Typically, Raman spectroscopy is effective in investigating the structure defects in graphene by monitoring the D- and G-band.[27] The D-band peak, which occurs at ~1330 cm^{-1}, is the finger print of defects since it is associated with hexagonal framework defects or sp^3 carbon, while the G-band peak at ~1580 cm^{-1} is due to the in-plane bond stretching motion of sp^2 carbon. Besides, the spectra also exhibited another characteristic 2D-band peak appeared at ~2670 cm^{-1}. The interaction between graphene and polymer networks could be estimated by the intensity ratio of the D- and G-bands (I_D/I_G), where I_D and I_G were the integrated intensities calculated from fitted spectra curves using Lorentzian lineshapes parameters.[28,29] As shown in **Fig. 5(a)**, the composites displayed the prominent peaks at ~1330 cm^{-1}, ~1580 cm^{-1}, ~2670 cm^{-1} and some characteristic peaks of polymer structure. Since the I_D/I_G ratio increased dramatically from 0.78 of pristine graphene to 1.65 of 0.4-GEP, it could be assumed a portion of sp^2-domain carbon of graphene transformed to sp^3-domain to form covalent bonds with polymer networks during polymerization, which gave rise to the appearance of D-band peak on graphene and developed strong interactions between the polymer chains and graphene.[30,31] The peak positions of the G-band were not shifted appreciably and the positions of D-band and 2D-band showed shifts by ~6 cm^{-1} compared to the pristine graphene, which was probably because the polymer chains anchored on the graphene. This strong chemical interaction increased the energy necessary for vibrations to occur, which is reflected in the higher frequency of the Raman peaks.[32] **Fig. 5(b)** showed Raman spectra comparison of the composites with different contents of graphene. The I_D/I_G ratio was calculated to be 1.65, 1.13 and 1.05 for 0.4-GEP, 0.7-GEP and 1.0-GEP, respectively. Graphene of 1.0 wt% content could chemically interact with polymer networks to some extent as 0.4-GEP and 0.7-GEP samples. However, it also dispersed in form of agglomeration state in the polymer matrix, as depicted in **Fig. 2** and **Fig. 3**. Therefore, the Raman spectra indicated an optimum content of graphene in a polymer matrix when graphene was introduced in the suspension polymerization. From the viewpoint of Raman spectra and SEM images, it can be assumed that during the suspension polymerization of 0.4-GEP, graphene could effectively tether with the polymer chain radicals or initiator fragments and penetrate into the polymer networks,[13,33] which leads to well dispersion of graphene in the polymer matrix and enhanced interaction between the graphene and the polymer networks.

The FTIR spectra were shown in **Fig. 6**. After chloromethylation, the samples showed the absorption peaks at 1265 cm^{-1} and 677 cm^{-1}, which were attributed to the in-plane bending vibration of aromatic C-H in Ph-CH$_2$Cl groups and C-Cl stretching vibration.[34] Concomitantly, the weak shoulder peaks at ~1421 cm^{-1} were assigned to the bending vibration of C-H in chloromethyl groups (-CH$_2$Cl). After amination, all the chlorine-containing groups disappeared and new peaks at ~976 cm^{-1} attributed to C-N stretching were clearly observed. Besides, the peaks at ~1635 cm^{-1} corresponded to O-H in-plane bending vibration. These results confirmed the existence of -N$^+$(CH$_3$)$_3$OH$^-$ groups grafted on the polymer chains in successful chloromethylation and amination step.[13,35,36] After ion exchange process, the strong absorption bands were observed at ~1280 cm^{-1} in PS-DVB-HC and 0.4-GEP-HC, which were attributed to the stretching vibration of C-O in bicarbonate groups.

To further understand the carbonaceous species in the polymer, the fitting XPS curves of the core-level C$_{1s}$ spectra were plotted in **Fig. 7**. **Table 1** summarized the detailed atomic composition of the surface C and O. Some trace amounts of other elements were not shown in the table. Since the XPS experiments were carried out with degassing overnight, the presence of surface O is a reference variable in the results which may be derived from the functional group on the IERs surface introduced by amination step and absorbed moisture. 0.7-GEP-OH showed the highest level of 12.49% surface O atomic composition, indicating the highest value of -OH group in the amination product. The C$_{1s}$ core-level spectra were deconvoluted into three peaks at the binding energy of ~284.8 eV, ~286.2 eV and 288.0 eV, which could be assigned to the sp^2 C=C/sp^3 C-C, -C-O and -C=O components.[37-39] It could be seen that the addition of graphene largely suppressed the binding energy intensity of sp^2 C=C/sp^3 C-C, while that associated with -C-O species increased accordingly. The increased surface -C-O/-C-C ratios of GPNC-IERs with 0.1-0.7 wt% confirmed the successful functionalization process of well dispersed nanocomposites. 1.0-GEP-OH sample exhibited a decrease in O/C and -C-O/-C-C ratios on the surface, which was highly consistent with SEM and Raman results.

The physical properties of the GPNC-IERs were listed in **Table 2**. To determine the values of the water retention capacity, total exchange capacity and swelling capacity, all the samples were measured at least twice. The structural properties of GPNC-IERs resembled the PS-DVB-HC, including average mesh density and mean mesh size. Although the composites contained different contents of graphene in the polymer networks, the fundamental structures of the IERs were nearly identical. However, the structural properties, such as total exchange capacity and swelling capacity, were highly influenced by the graphene contents. In good solvent such as THF, the swelling capacity dropped rapidly with the increasing graphene content. Besides, it was found that small amounts of graphene dramatically improved the total exchange capacity behavior. Among these GPNC-IERs, 0.4-GEP-HC and 0.7-GEP-HC showed the higher value at 1.88 and 1.91 mmol·g^{-1}. This result could be explained by the fact that the high level electron cloud density in graphene might produce π-π conjugative effect between graphene and adjacent aromatic structure of styrene, and favor the electrophilic substitution reaction of chloromethylation process, providing more reactive sites for functional groups, as shown in **Scheme 1**. From the morphology of 1.0-GEP-HC shown in **Fig. 2**, some graphene aggregated in the nanocomposite without chemically bonded with polymer chains. This might be the reason that 1.0-GEP-HC showed slight decrease in total exchange capacity compared to 0.7-GEP-HC. It should be noted that the exchange capacity was related to the total basic alkaline content of the HCO_3^- group. Therefore, the nanocomposites with 0.4 wt% and 0.7 wt% graphene had the higher level of basic content, which was consistent with the XPS results.

The TGA-DTA of the GPNC and GPNC-IERs were measured and depicted in **Fig. 8**. As observed in the TGA curves, pristine graphene exhibited a high thermal stability with the initial decomposition temperature at 637.8 °C and the maximum weight loss rate occurred around 722.0 °C. PS-DVB-HC exhibited three degradation steps occurring at the temperature ranges of 100-200 °C, 200-450 °C and 450-600 °C, respectively. The initial 10% weight loss was due to the elimination of the moisture in the samples at the first stage. Then PS-DVB-HC showed a major weight loss stage about 70%, which was due to the degradation of the branching chains and crosslinking networks to short chains or volatile compounds induced by oxidative atmosphere.[20,40,41] The third stage weight loss of 20% was assigned to the combustion of char residue of carbonaceous to volatile fragments (such as CO_2 and water), and all the samples completely burnt off at 600 °C. In the case of GPNC-IERs, the last stage showed higher amount of char residue compared to the PS-DVB-HC, which was related to the decomposition/combustion of graphene and the residue of carbonaceous. The extrapolated degradation onset temperatures (T_d) and the temperature of the maximum weight loss rate (T_{max1} and T_{max2}) in **Table 3** showed the effect of graphene content on the degradation behavior and thermal stability of the GPNC-IERs. The increase in T_d and T_{max} indicated the enhancement in the thermal stability of GPNC-IERs. PS-DVB-HC reached the maximum weight loss velocity at 417.7 °C. The T_d and T_{max} of the GPNC-IERs all shifted to higher temperature, especially for 0.4-GEP-HC and 0.7-GEP-HC, it increased by ~20 °C compared to PS-DVB-HC.

A thermal transition of a segmental motion of the polymer chains was examined and the glass transition temperature (T_g) obtained by DSC measurements were also summarized in **Table 3**. In the case of pure PS-DVB-HC, T_g was at 89.6 °C and slightly increased by 3 °C for 0.4-GEP-HC.

Catalytic hydration of ethylene oxide on the GPNC-IER catalysts

The characterization results confirmed the enhanced anti-swelling capacity and thermal stability of GPNCs and GPNC-IERs and the amounts of surface quaternary ammonium group increased as well. In particular, the structural and thermal stability were improved significantly in the nanocomposites with 0.4 wt% and 0.7 wt% graphene. Normally, the resin catalyst stability is the critical factor to restrict the application because the resins swell and deactivate under the reaction conditions. These improved GPNC-IER resin catalysts were applied in catalytic hydration of EO.

As seen in **Fig. 9**, the EO conversion of all the IER catalysts increased with the temperature up to 102 °C, whereas the MEG selectivity slightly decreased at higher temperature. This was quite similar to the result reported by Yu *et al.*.[13] Although high temperature could accelerate hydration reaction rate with high EO conversion, it was likely that the decrease of MEG selectivity was due to the side reactions in the circumstance of higher MEG concentration with elevated temperature.[1,2,42] On the other hand, the MEG selectivity was also influenced by the undesirable swelling and thermal deactivation of the IER catalysts during reaction. The quaternary ammonium groups on the IER catalysts surface were the active sites for the hydration of EO *via* the ring-opening reaction, and high water/EO molar ratio was normally used for obtaining high MEG selectivity. The IER catalysts were inevitable to be affected and undergo thermal degradation and swelling even at a low water/EO molar ratio of 10, thus resulting in low MEG selectivity. According to the aforementioned results, the higher values of [HCO_3^-] and [OH^-] in the GPNC-IERs facilitated the hydration reaction with higher EO conversion. Meanwhile, good graphene dispersion and graphene-polymer network facilitated heat transfer and allowed the heat of the reaction to travel efficiently through the polymer matrix and graphene. Therefore, the GPNC-IERs maintained stable under the reaction conditions because of the improved anti-swelling capacity and thermal stability.

Xie *et al.*[17] have reported the enhanced performance of polymer/CNTs composites in the EO hydration reaction test. For comparison, the EO hydration reaction results of CNTs-based polymer nanocomposites ion-exchange resins (CPNC-IERs) and GPNC-IERs were shown in **Fig. 10**. The 0.4-CNTP-HC was prepared by the same procedure as 0.4-GEP-HC, except the CNTs as a reinforcing material in the polymer nanocomposites. The EO conversion and MEG selectivity for 0.4-GEP-HC exhibited better performance at a range of 90-102 °C. These results indicate that the enhancement in properties and reactive performance of graphene-based nanocomposites is markedly superior to the effect of the CNTs in the polymer matrix.[20]

The long-time run of the IER catalysts in the hydration of EO at 98 °C was carried out for 500 h on stream, and the results were plotted in **Fig. 11**. It was found that the EO conversion and MEG yield for 0.4-GEP-HC remained at 98% and 95%, which were much higher than the conventional PS-DVB-HC catalyzed system during the whole 500 h test, allowing a large window for the industrial application in the hydration of EO in the future. Additionally, the MEG yield on the conventional PS-DVB-HC gradually decreased to ~89% after 500 h reaction test. This was likely due to the thermal deactivation of the active groups on the catalysts resulting in lower activity and selectivity. The total exchange capacity of the IER catalysts were measured again after 500 h hydration test, the data in **Table 4** confirmed that the addition of graphene in the IER catalysts was beneficial to improve the stability of the surface active sites.

Effect of graphene in the nanocomposites

In this work, graphene was applied as a reinforcing material in the polymer nanocomposites synthesized *via in situ* suspension polymerization. The pre-suspension procedure was used for assisting the formation of uniform polymer beads. The results showed that graphene could be well dispersed in the composites, and the strong interaction between graphene and polymer cross-linked networks was demonstrated here to be an important factor to the enhancement effects in thermal stability and anti-swelling properties of the composites.

It is generally accepted that two main approaches, “grafting-from” and “grafting-to”, have been developed to introduce graphene into the polymer structures. It is worth noting that the GPNCs are obtained by both methodologies. At the beginning of polymerization, the initiator BPO generates phenyl radicals, which can lead to a functionalization reaction on graphene sheets. The resulting radical functionalized graphene could subsequently react with the adsorbed styrene monomer molecule. With covalent bonding with free radical and styrene, a portion of the sp^2 carbon on graphene is converted to sp^3 carbon leading to an increase in D-band peak intensity in Raman spectra. Mylvaganam *et al.*[43] showed by computation that free radical functionalized graphene could initiate the polymerization reaction with chemically bonded polymer chains growing on graphene. Based on this “grafting-from” methodology, the polymeric fragment is propagated from graphene surface by capturing more styrene molecules.[33,44] Meanwhile, based on the “grafting-to” methodology, polymer chain with free radical, like $[\text{-CH}_2\text{-CH(Ph)-...-CH}_2\text{-CH(Ph)}]\bullet$ can be directly conjugated with graphene , which allows further conjugation of a new monomer molecule or polymer chain. This chain propagation prefers to occur on the opposite side of graphene sheet to avoid steric hindrance, which appears like graphene incorporated into the polymer networks. The growing polymer chains will terminate through combining with another propagating polymer chain or radical functionalized graphene directly.

In the as-prepared polymer composites, graphene acts as covalent cross-linkers to form the polymer networks improving interfacial interaction with polymer chains. Moreover, the well dispersed graphene can induce the barrier labyrinth effect, impeding the transport of degradation products of polymer into the gas phase. More energy is required to break the covalent linkages and transport the degradation products of polymer, which tends to shift the T_d and T_max to higher temperatures. As described above, graphene can chemically incorporated into the polymer networks, which introduces the steric limitation through the resin and restricts the polymer chain mobility in the nanocomposites, resulting in higher T_g value.[19,44] Therefore, it may be concluded that covalent bonded graphene *via* direct polymerization herein effectively protects against thermal degradation and transition for the polymer networks, providing enhanced structural and thermal stability of GPNCs and GPNC-IERs.

To better demonstrate the graphene-polymer synergism in thermal stability, dynamic FTIR spectra of 0.4-GEP-OH and PS-DVB-OH at different temperatures in N_2 were recorded and presented in **Fig. 12**. The peaks observed in the region of 3025-3080 cm^{-1} and 2920-2850 cm^{-1} were attributed to the stretching vibrations of the aromatic C-H and the C-H stretching vibrations of the methylene groups. The broad absorption peaks at 3420 cm^{-1} and 1633 cm^{-1} could be assigned to the stretching vibration and in-plane bending vibration of associative -OH group.[35] During heating up process, the intensity of these peaks decreased slowly, indicating the C-H and -OH dissociated with the elevated temperature to 200 °C. The obvious diminution in peak intensity at 1310 cm^{-1} implied the thermal decomposition of C-N groups.[45] The gradual peak intensity decrease of 1450-1600 cm^{-1} from 150-400 °C could infer that the aromatic C=C of the carbon skeleton decomposed to some volatile fragments, leading to the disappearance of the absorption band at 450 °C. As for 0.4-GEP-OH, shown in **Fig. 12(b)**, the distinct peak intensity decrease at 3420 cm^{-1} and 1640 cm^{-1} were assigned to the initial dissociation of the quaternary ammonium hydroxide groups ($\text{-N}^+(\text{CH}_3)_3\text{OH}^-$) with the elevated temperature to 250 °C, which showed the ~50 °C improvement in thermal stability of functional groups. Besides, the absorption band at 1410 cm^{-1} was assigned to the C-H in-plane bending vibration of $\text{-CH}_2\text{-N}^+$ groups, which decreased and disappeared until 250 °C, confirming the decomposition of the functional groups on the GPNC-IERs at higher temperature.[46]

Scheme 2 depicted the initial thermal degradation steps of the PS-DVB-OH and 0.4-GEP-OH samples. It is well accepted that quaternary ammonium hydroxides ($\text{-N}^+(\text{CH}_3)_3\text{OH}^-$) undergo thermal degradation to produce a tertiary amine and an alcohol. The two possible degradation ways result in either a basic group or a non-active benzyl alcohol.[47] PS-DVB-OH preferred to decompose started by breaking the $\text{-CH}_2\text{-N}^+$ bond, producing a benzyl alcohol structure. The degradation of 0.4-GEP-OH occurred preferentially by -OH group dissociation and obtained a weak basic anion exchange resin, as shown in **Scheme 2(b)**. The present of weak basic anion of $\text{-N}^+(\text{CH}_3)_2$ on the exchange resins could prevent the deactivation of IER catalysts, which further confirmed the catalytic reaction results.

Overall, the addition of graphene to PS-DVB polymer resin performed an enhanced thermal stability and anti-swelling capacity. More attractively, Raman spectra showed that graphene tends to form a covalent bond with the polymer chains at the reactive sites on the graphene sheets, and/or assembles a 3D-network stability through the polymer resin, suggesting good interfacial compatibility between the graphene and the entangled polymer chains. The incorporated graphene functions as an effective barrier to inhibit the mass loss and retards the transfer of degradation products of the polymer into the gas phase, enabling the higher thermal degradation temperatures.[40,44,48,49] Detailed information of the TG-DTA and dynamic FTIR results demonstrated that graphene mainly affect the degradation of functional groups and cross-linked polymer networks of the IERs. It is noteworthy that the composites with 0.1-0.7 wt% graphene exhibited enhancements in total exchange capacity and resistance to thermal degradation. However, the composite containing 1.0 wt% graphene exhibited the opposite behavior, especially T_max1 and T_g. Therefore, the graphene concentration in the composites is not the only factor for the changes in the properties. Considering the morphology results shown in **Fig. 2** and **Fig. 3**, graphene was well distributed all over the polymer surface at low concentrations, while 1.0-GEP showed some great irregularity and rupture on the surface. The aggregation of graphene accounts for a suppression in the enhancement effect because of reduction of effective interfacial area between the graphene and polymer networks.

As elaborated above, the nanocomposites with 0.7 wt% graphene showed the best properties among these prepared samples. However, whether 0.7 wt% of graphene in the polymer resin manifests the optimum performance in these structural properties is not clear yet. Nonetheless, the total exchange capacity of the GPNC-IER is not in a simple positive correlation with graphene contents from 0.1-1.0 wt%, but a 'volcano-type' scatter similar to the results reported by Malho *et al.*.[50] At graphene content of 1.0 wt%, the properties are even slightly poorer than the composites with 0.4 wt% graphene. Such a 'volcano-type' trend on water retention capacity, exchange capacity, anti-swelling property and thermal stability might be attributed to the dispersion of graphene within the composite structures and the interaction between graphene-polymer networks,[51] which is consistent with the mechanism proposed previously. Considering this trend in the GPNC-IERs, it might need further study in order to exploit the optimum graphene concentration for the composites' properties.

Conclusions

In summary, we have demonstrated a generic approach to prepare GPNCs by modified surfactant-free *in situ* suspension polymerization. The direct use of graphene to react with styrene monomer could produce the GPNCs with good dispersion of graphene and strong interaction within the polymer matrix. The structural and thermal stability of the GPNCs and GPNC-IERs were improved greatly with incorporation of graphene in the polymer networks. With a low content at 0.4 wt% of graphene, the strong basic GPNC-IERs showed enhanced activity and selectivity performance in catalytic hydration of EO to MEG. The long-term reaction test further confirmed that graphene effectively reinforced the properties with well incorporation into the polymer networks.

Acknowledgements

This work was supported by Science and Technology Commission of Shanghai Municipality, China (13R21421900).

Notes and references

[a] *SINOPEC Shanghai Research Institute of Petrochemical Technology, Shanghai 201208, PR China. E-mail: yangwm.sshy@sinopec.com.*

† Electronic Supplementary Information (ESI) available: [details of any supplementary information available should be included here]. See DOI: 10.1039/b000000x/

1 Z.-J. Yang, N. Ren, Y.-H. Zhang and Y. Tang, *Catal. Commun.*, 2010, **11**, 447-450.
2. H. Yue, Y. Zhao, X. Ma and J. Gong, *Chem. Soc. Rev.*, 2012, **41**, 4218-4244.
3. M. R. Altiokka and S. Akyalçin, *Ind. Eng. Chem. Res.*, 2009, **48**, 10840-10844.
4. V. F. Shvets, R. A. Kozlovskiy, I. A. Kozlovskiy, M. G. Makarov, J. P. Suchkov and A. V. Koustov, *Chem. Eng. J.*, 2005, **107**, 199-204.
5. V. F. Shvets, R. A. Kozlovskiy, I. A. Kozlovskiy, M. G. Makarov, J. P. Suchkov and A. V. Koustov, *Org. Process Res. Dev.*, 2005, **9**, 768-773.
6. G. R. Strickler, V. G. Landon, G.-S. J. Lee and W. J. Rievert, 1999, **WO Patent**, **9931034**.
7. G. H. Grosch, B. Stein and E. Gehrer, 1999, **DE Patent**, **19757684**.
8. K. Kawabe, 2000, **US Patent**, **6080897**.
9. E. M. G. A. V. Kruchten, 1999, **US Patent**, **5874653**.
10. Y. Li, B. Yue, S. Yan, W. Yang, Z. Xie, Q. Chen and H. He, *Catal. Lett.*, 2004, **95**, 163-166.
11. C.-F. Lien, C.-H. Ho, C.-Y. Shieh, C.-L. Tseng and J.-L. Lin, *J. Phys. Chem. C*, 2008, **112**, 8365-8371.
12. Z.-J. Yang, Y.-F. Li, Q.-B. Wu, N. Ren, Y.-H. Zhang, Z.-P. Liu and Y. Tang, *J. Catal.*, 2011, **280**, 247-254.
13. F. Yu, H. Cai, W. He, W. Yang and Z. Xie, *J. Appl. Polym. Sci.*, 2010, **115**, 2946-2954.
14. E. J. Simpson, W. J. Koros and R. S. Schechter, *Ind. Eng. Chem. Res.*, 1996, **35**, 1195-1205.
15. A. R. Vaino and K. D. Janda, *J. Comb. Chem.*, 2000, **2**, 579-596.
16. T. Ghosh Dastidar and A. Netravali, *ACS Sustainable Chem. Eng.*, 2013, **1**, 1537-1544.
17. Z. Xie, Z. Liu, Y. Wang, Q. Yang, L. Xu and W. Ding, *Int. J. Mol. Sci.*, 2010, **11**, 2152-2187.
18. P. A. Denis, *J. Phys. Chem. C*, 2009, **113**, 5612-5619.
19. J. R. Potts, D. R. Dreyer, C. W. Bielawski and R. S. Ruoff, *Polymer*, 2011, **52**, 5-25.
20. Y. Li, F. Yu, W. He and W. Yang, *J. Appl. Polym. Sci.*, 2014, 10.1002/app.41234.
21. X. Qian, L. Song, B. Yu, B. Wang, B. Yuan, Y. Shi, Y. Hu and R. K. K. Yuen, *J. Mater. Chem. A*, 2013, **1**, 6822-6830.
22. Y. Jing, H. Tang, G. Yu and P. Wu, *Polym. Chem.*, 2013, **4**, 2598-2607.
23. W. Hu, J. Zhan, X. Wang, N. Hong, B. Wang, L. Song, A. A. Stec, T. R. Hull, J. Wang and Y. Hu, *Ind. Eng. Chem. Res.*, 2014, **53**, 3073-3083.
24. J.-M. Thomassin, M. Trifkovic, W. Alkarmo, C. Detrembleur, C. Jérôme and C. Macosko, *Macromolecules*, 2014, **47**, 2149-2155.
25. S. Bhuyan, S. Sundararajan, D. Andjelkovic and R. Larock, *Tribol. Int.*, 2010, **43**, 831-837.
26. Y. Huang, M. Zeng, J. Ren, J. Wang, L. Fan and Q. Xu, *Colloids Surf., A*, 2012, **401**, 97-106.
27. D. Fan, Y. Liu, J. He, Y. Zhou and Y. Yang, *J. Mater. Chem.*, 2012, **22**, 1396-1402.
28. S. Sahoo, R. Palai, S. K. Barik and R. S. Katiyar, *J. Raman Spectrosc.*, 2013, **44**, 798-802.
29. M. S. Dresselhaus, A. Jorio, A. G. Souza Filho and R. Saito, *Philos. Trans. R. Soc. A*, 2010, **368**, 5355-5377.
30. M. Fang, K. Wang, H. Lu, Y. Yang and S. Nutt, *J. Mater. Chem.*, 2009, **19**, 7098-7105.
31. V. Georgakilas, M. Otyepka, A. B. Bourlinos, V. Chandra, N. Kim, K. C. Kemp, P. Hobza, R. Zboril and K. S. Kim, *Chem. Rev.*, 2012, **112**, 6156-6214.
32. R. Asif, D. D. Mark, I. Ilia, F. B. Phillip and B. G. David, *Chem. Mater.*, 2006, **18**, 3513-3522.
33. J. Park and M. Yan, *Acc. Chem. Res.*, 2013, **46**, 181-189.
34. Y. Cao, Z. Lai, J. Feng and P. Wu, *J. Mater. Chem.*, 2011, **21**, 9271-9278.
35. Y. Zhao, M. Seredych, Q. Zhong and T. J. Bandosz, *RSC Adv.*, 2013, **3**, 9932-9941.
36. K. Kunimatsu, B. Bae, K. Miyatake, H. Uchida and M. Watanabe, *J. Phys. Chem. B*, 2011, **115**, 4315-4321.
37. R. Haerle, E. Riedo, A. Pasquarello and A. Baldereschi, *Phys. Rev. B*, 2001, **65**, 045101-045101-045101-045109.
38. Z. J. Han, B. K. Tay, P. C. T. Ha, J. Y. Sze and D. H. C. Chua, *J. Appl. Phys.*, 2007, **101**, 053301-053301-053301-053307.
39. W.H. Lee, S.J. Kim, W.J. Lee, J.G. Lee, R.C. Haddon and P. J. Reucroft, *Appl. Surf. Sci.*, 2001, **181**, 121-127.
40. F. Laoutid, L. Bonnaud, M. Alexandre, J. M. Lopez-Cuesta and P. Dubois, *Mater. Sci. Eng. R*, 2009, **63**, 100-125.
41. S. Navalon, A. Dhakshinamoorthy, M. Alvaro and H. Garcia, *Chem. Rev.*, 2014, **114**, 6179-6212.
42. J. W. van Hal, J. S. Ledford and X. Zhang, *Catal. Today*, 2007, **123**, 310-315.

43. K. Mylvaganam and L. Zhang, *J. Phys. Chem. C*, 2013, **117**, 2817-2823.
44. A. S. Patole, S. P. Patole, S.-Y. Jung, J.-B. Yoo, J.-H. An and T.-H. Kim, *Eur. Polym. J.*, 2012, **48**, 252-259.
45. S. Ramalingam, S. Periandy, B. Narayanan and S. Mohan, *Spectrochim. Acta. A*, 2010, **76**, 84-92.
46. A. Danon, P. C. Stair and E. Weitz, *J. Phys. Chem. C*, 2011, **115**, 11540-11549.
47. G. C. Allen, N. R. Holmes, B. J. Lee and R. R. Harries, *J. Chem. Soc. Faraday Trans.*, 1988, **84**, 3891-3904.
48. Kashiwagi Takashi , Grulke Eric, Hilding Jenny , Harris Richard, Awad Walid and D. Jack, *Macromol. Rapid Commun.*, 2002, **23**, 761-765.
49. O. Hyunjoon and P. F. Green, *Nat. Mater.*, 2009, **8**, 139-143.
50. J.-M. Malho, P. Laaksonen, A. Walther, O. Ikkala and M. B. Linder, *Biomacromolecules*, 2012, **13**, 1093-1099.
51. R. Rahman, J. T. Foster and A. Haque, *J. Phys. Chem. A*, 2013, **117**, 5344-5353.

Captions

Scheme 1 Schematic diagram of reaction steps involved in the preparation of GPNC-IERs.

Scheme 2 Schematic diagram of the initial thermal degradation steps of (a) PS-DVB-OH and (b) 0.4-GEP-OH samples.

Fig. 1 Photographs of graphene dispersions in styrene: (a) [graphene]=0.09 mg·mL^{-1}; (b) [graphene]=0.42 mg·mL^{-1}; (c) [graphene]=0.66 mg·mL^{-1}; (d) [graphene]=0.98 mg·mL^{-1}.

Fig. 2 SEM images of PS-DVB and GPNC-IERs in bicarbonate form: (a) PS-DVB; (b) 0.1-GEP; (c) 0.4-GEP; (d) 0.7-GEP; (e) 1.0-GEP; (f) PS-DVB-HC; (g) 0.1-GEP-HC; (h) 0.4-GEP-HC; (i) 0.7-GEP-HC; (j) 1.0-GEP-HC.

Fig. 3 TEM images of pristine graphene and 0.4-GEP nanocomposites.

Fig. 4 Raman spectra of pristine graphene, PS-DVB and GPNCs.

Fig. 5 FTIR spectra of PS-DVB and GPNC-IERs.

Fig. 6 Core-level C_{1s} XPS spectra of PS-DVB and GPNC-IERs: (a) PS-DVB-OH; (b) 0.1-GEP-OH; (c) 0.4-GEP-OH; (d) 0.7-GEP-OH; (e) 1.0-GEP-OH.

Fig. 7 TG-DTA curves of PS-DVB and GPNC-IERs: (a) PS-DVB-HC; (b) 0.4-GEP-HC; (c) 0.7-GEP-HC; (d) pristine graphene.

Fig. 8 Catalytic performance of PS-DVB-HC, 0.4-GEP-HC and 0.7-GEP-HC for the hydration of EO.

Fig. 9 Catalytic performance of PS-DVB-HC and 0.4-GEP-HC catalysts within 500 h.

Fig. 10 FTIR spectra in N_2 atmosphere of (a) PS-DVB-OH and (b) 0.4-GEP-OH.

Table 1 Surface atomic composition of the GPNC-IERs and PS-DVB IER samples in hydroxylic form.

Table 2 Physical properties of the GPNC-IERs and PS-DVB IER samples.

Table 3 Thermal properties of the GPNC-IERs and PS-DVB IER samples.

Table 4 Reaction results of the GPNC-IERs and PS-DVB IER catalysts at 98 °C.

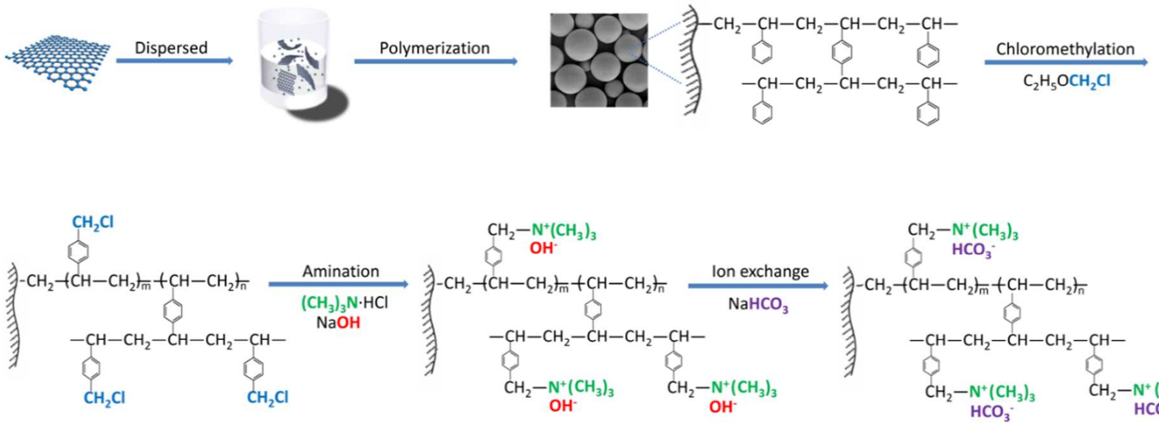

Scheme 1 Schematic diagram of reaction steps involved in the preparation of GPNC-IERs.

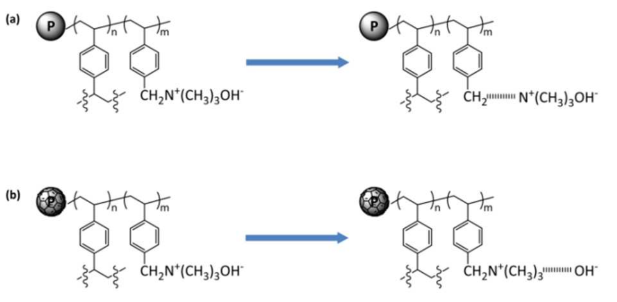

Scheme 2 Schematic diagram of the initial thermal degradation steps of (a) PS-DVB-OH and (b) 0.4-GEP-OH samples.

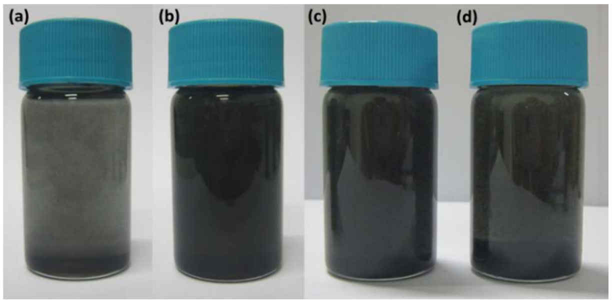

Fig. 1 Photographs of graphene dispersions in styrene: (a) [graphene]=0.09 mg·mL^{-1}; (b) [graphene]=0.42 mg·mL^{-1}; (c) [graphene]=0.66 mg·mL^{-1}; (d) [graphene]=0.98 mg·mL^{-1}.

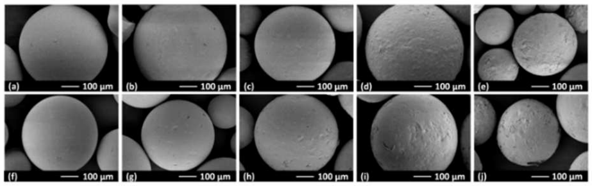

Fig. 2 SEM images of PS-DVB and GPNC-IERs in bicarbonate form: (a) PS-DVB; (b) 0.1-GEP; (c) 0.4-GEP; (d) 0.7-GEP; (e) 1.0-GEP; (f) PS-DVB-HC; (g) 0.1-GEP-HC; (h) 0.4-GEP-HC; (i) 0.7-GEP-HC; (j) 1.0-GEP-HC.

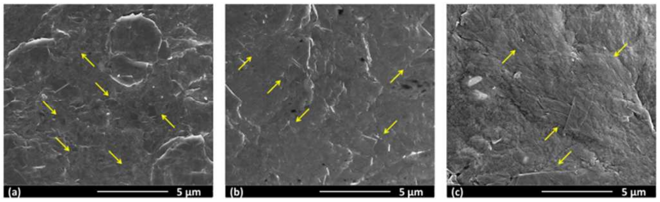

Fig. 3 SEM images of fracture surface of GPNCs: (a) 0.4-GEP; (b) 0.7-GEP; (c) 1.0-GEP.

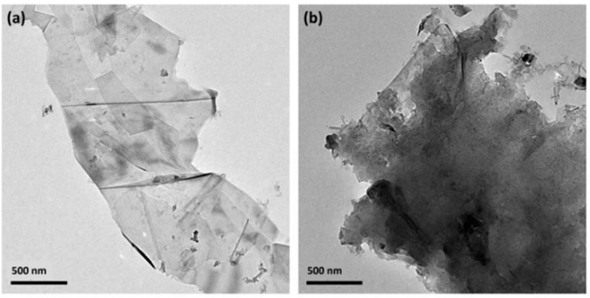

Fig. 4 TEM images of pristine graphene and 0.4-GEP nanocomposites.

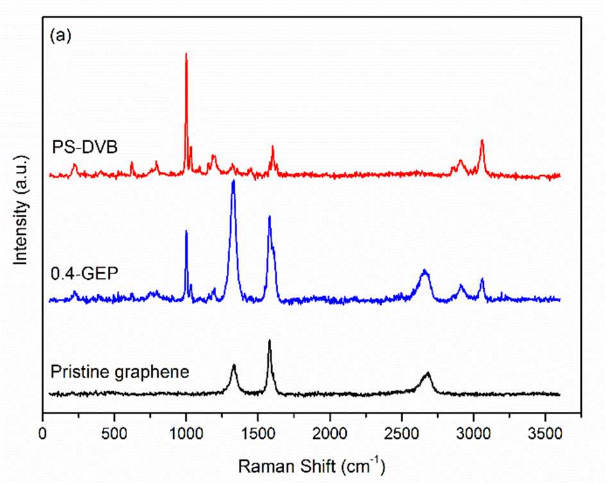

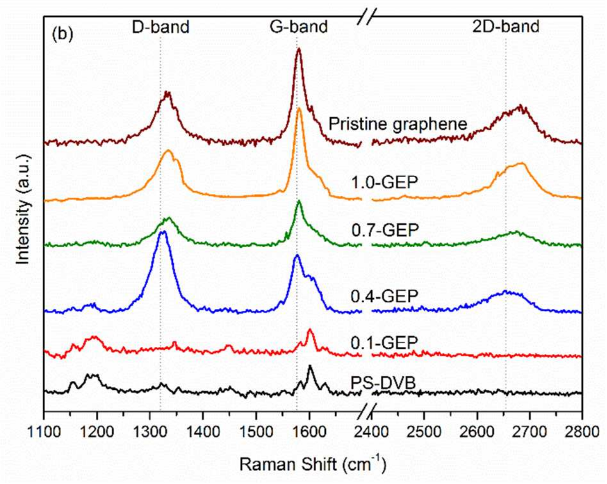

Fig. 5 Raman spectra of pristine graphene, PS-DVB and GPNCs.

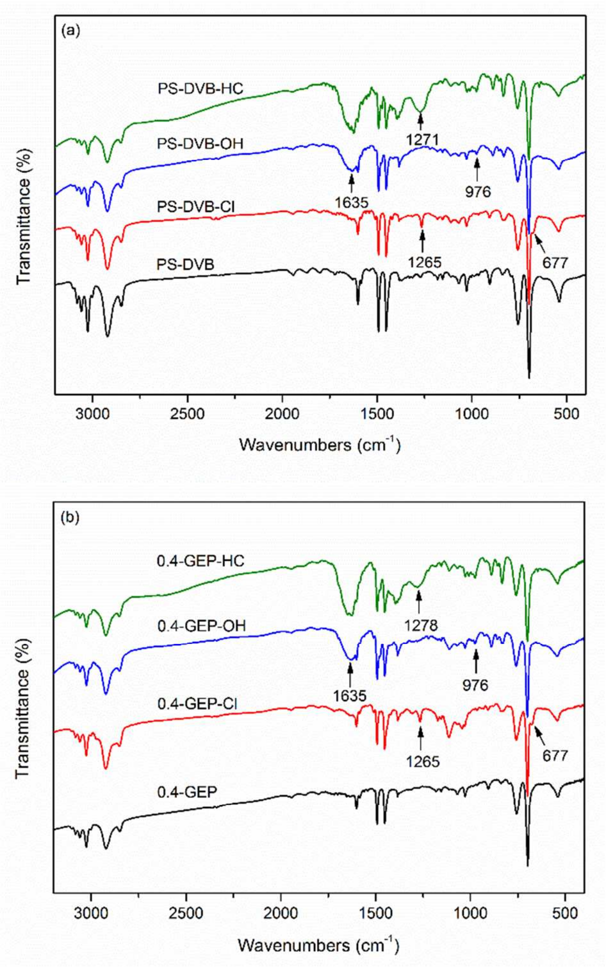

Fig. 6 FTIR spectra of PS-DVB and GPNC-IERs.

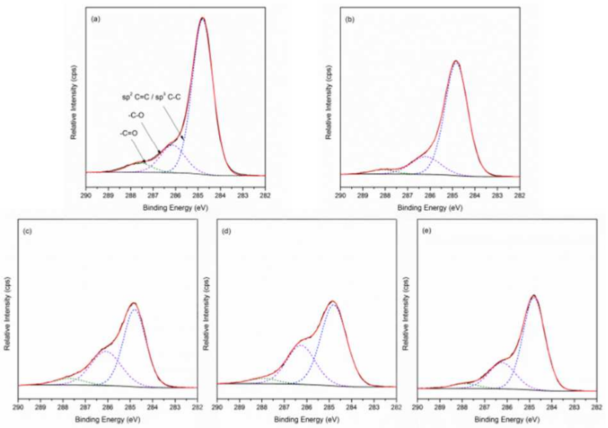

Fig. 7 Core-level C_{1s} XPS spectra of PS-DVB and GPNC-IERs: (a) PS-DVB-OH; (b) 0.1-GEP-OH; (c) 0.4-GEP-OH; (d) 0.7-GEP-OH; (e) 1.0-GEP-OH.

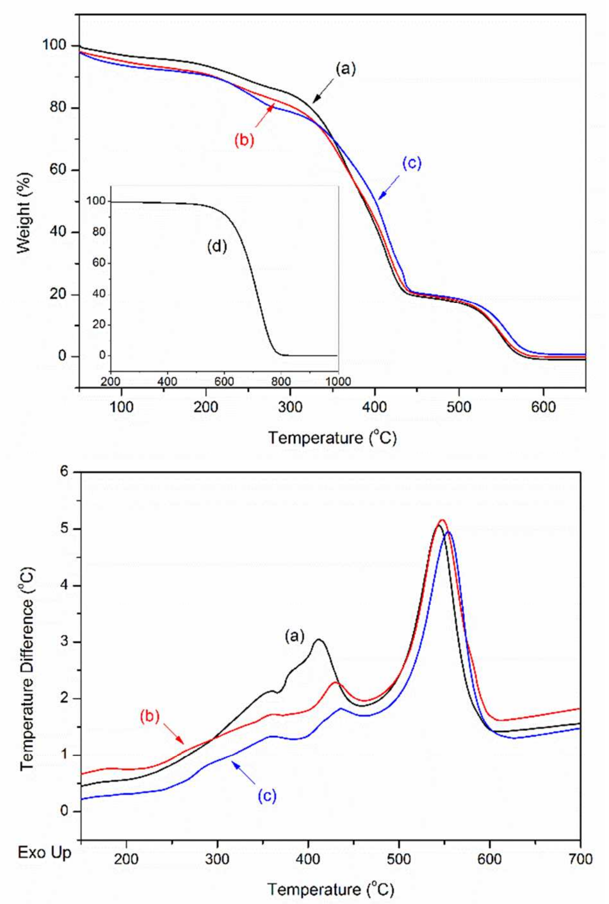

Fig. 8 TG-DTA curves of PS-DVB and GPNC-IERs: (a) PS-DVB-HC; (b) 0.4-GEP-HC; (c) 0.7-GEP-HC; (d) pristine graphene.

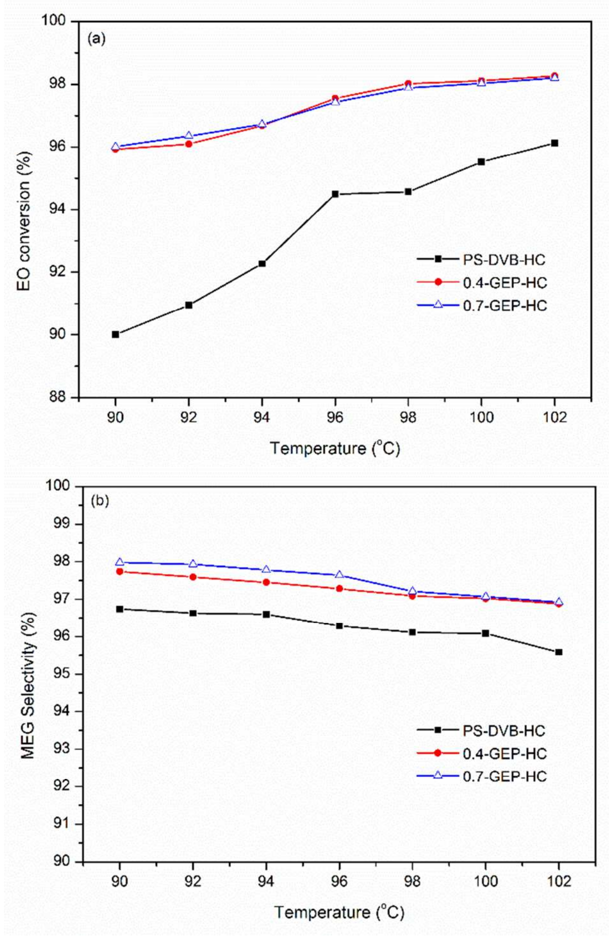

Fig. 9 Catalytic performance of PS-DVB-HC, 0.4-GEP-HC and 0.7-GEP-HC for the hydration of EO.

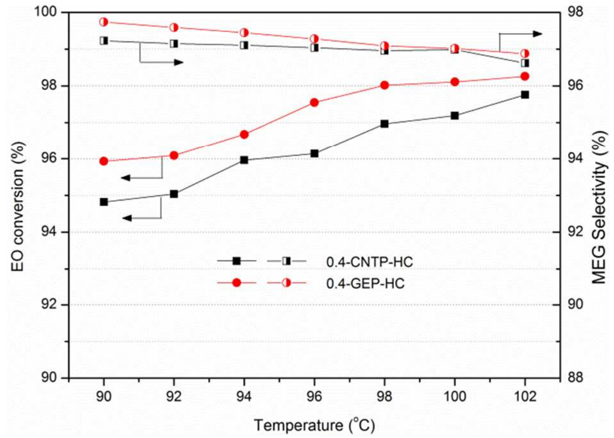

Fig. 10 Catalytic performance of 0.4-CNTP-HC and 0.4-GEP-HC for the hydration of EO.

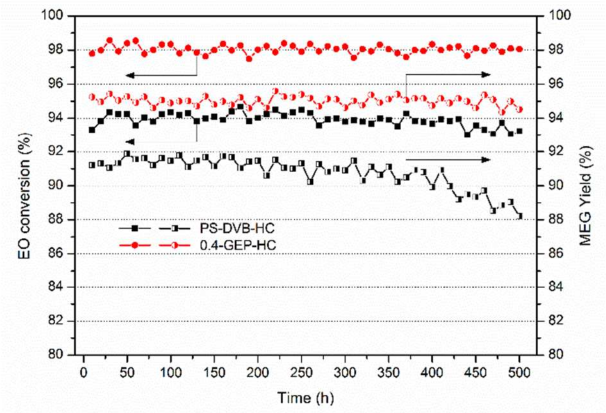

Fig. 11 Catalytic performance of PS-DVB-HC and 0.4-GEP-HC catalysts within 500 h.

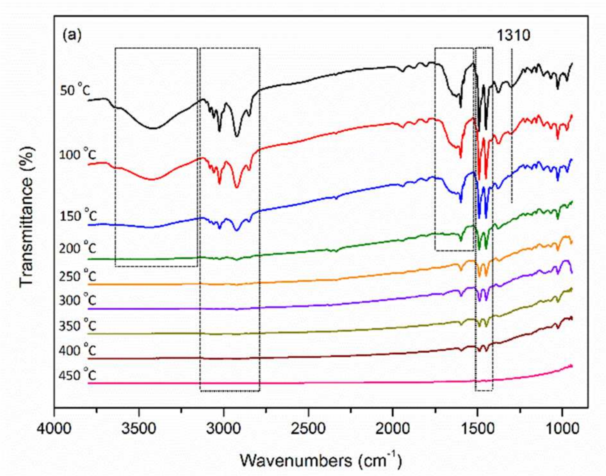

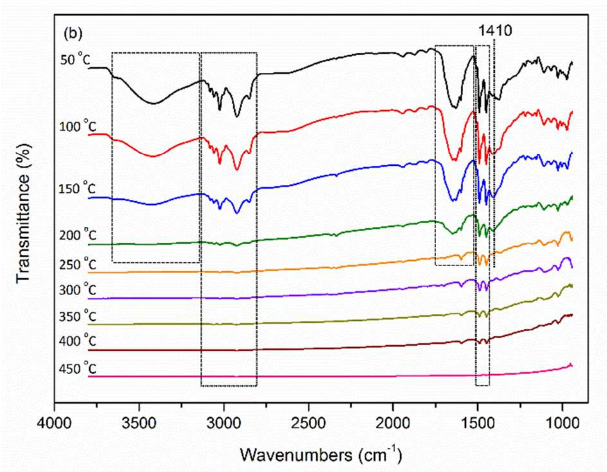

Fig. 12 FTIR spectra in N_2 atmosphere of (a) PS-DVB-OH and (b) 0.4-GEP-OH.

Table 1 Surface atomic composition of the GPNC-IERs and PS-DVB IER samples in hydroxylic form.

Samples	Surface atomic composition and ratio (%)			Surface covalent bonds ratio[a] (%)
	O_{1s}	C_{1s}	O/C ratio	-C-O/-C-C ratio
pristine graphene	1.83	97.87	1.9	2.1
PS-DVB-OH	6.61	89.28	7.4	21.2
0.1-GEP-OH	6.38	89.74	7.1	20.5
0.4-GEP-OH	11.96	83.17	14.4	47.6
0.7-GEP-OH	12.49	81.69	15.3	50.4
1.0-GEP-OH	7.12	89.88	7.9	34.2

a. Calculated by the area of fitting curves of the core-level C_{1s} spectra

Table 2 Physical properties of the GPNC-IERs and PS-DVB IER samples.

Samples	Mesh density[a] (ρ, g·cm^{-3})	Mean mesh size (D_v, nm)	Water retention capacity (A, %)	Total exchange capacity (Q, mmol·g^{-1})	Swelling capacity (*SC*, %)	
					Water	THF
PS-DVB-HC	0.53	0.44	21.1 ± 0.1	0.28	29.2	43.8
0.1-GEP-HC	0.53	0.43	19.9 ± 0.2	0.33	24.9	31.7
0.4-GEP-HC	0.54	0.54	39.8 ± 0.2	1.88	18.4	28.0
0.7-GEP-HC	0.56	0.57	40.2 ± 0.1	1.91	18.3	26.6
1.0-GEP-HC	0.57	0.54	28.7 ± 0.2	1.47	19.1	28.9

a. Measured by volume-weighted mean mesh density

Table 3 Thermal properties of the GPNC-IERs and PS-DVB IER samples.

Samples	T_d[a] (°C)	T_{max1}[b] (°C)	T_{max2}[b] (°C)	Char[c] (wt%)	T_g[d] (°C)

PS-DVB-HC	351.8	417.7	548.6	1.11	89.6
0.1-GEP-HC	360.0	429.5	549.3	1.24	90.8
0.4-GEP-HC	372.3	438.6	556.2	1.57	92.3
0.7-GEP-HC	375.8	441.3	560.0	1.79	91.7
1.0-GEP-HC	370.3	419.8	555.3	2.09	85.9

a. Determined by the extrapolated onset temperatures
b. Maximum weight loss temperatures in DTA curves
c. Determined from the TGA measurements in N_2 at 700 °C
d. Determined as the midpoint temperature at half the complete change of heat capacity in DSC curves

Table 4 Reaction results of the GPNC-IERs and PS-DVB IER catalysts at 98 °C.

Catalysts	EO conversion (X, %)	MEG selectivity (Y, %)	Time space yield of MEG (STY, g MEG·h^{-1}·g cat^{-1})	Total exchange capacity[a] (Q, mmol·g^{-1})
PS-DVB-HC	94.70	96.13	0.96	0.07
0.4-GEP-HC	98.05	97.03	1.32	0.76

a. Measured after 500 h reaction tests